Balanced Homodyne Interferometry for Quantum State Reconstruction

Timo Bracht

Contents

1 Introduction

1.1 Overall Goal

The goal of this bachelor thesis is to build an interferometer that is usable in an optical experiment using ultracold atomic gases. The idea is to reconstruct the wavefunction of light states that passed an ultra cold atomic cloud with the interferometer.

The long term goal of these kinds of experiments is the development of setups, that can process quantum information. Like any information processing, there is an input, processing and output.
Photons are one of the most promising carriers of quantum information, as it is possible to input information on photons, as light states can be precisly manipulated to encode information.
The processing of the information encoded in the photons is done with the aformentioned atomic clouds. These can act as logical gates, when the gas can be made into a non-linear medium. The atomic cloud in the main experiment, where the interferometer build in this thesis is later used, consists of Ytterbium. Ytterbium is used, because of it´s potential to form Rydberg blockades.
The interferometer is there, to readout the processed information and generate the output from that data. For that purpose a Mach-Zehnder Interferometer is built for homodyne balanced detection with 399 nm light. Other groups have used balanced homodyne detection, to reconstruct quantum states [7], [1], [5], [8].

In this thesis a Mach-Zehnder Interferometer is built based on a previous design, where some challenges were identified [11], [2]. The thesis will first go over the process of constructing and characterising the interferometer; then reconstructing the vacuum state with state tomography as a test for it´s ability to extract information from quantum states.

1.2 Desired Improvements for the Interferometer

The previous iteration of this setup identified the following challenges, which were approached in this thesis:

1. Size: The previous setup was too big to be implemented in an actual experiment with spatial limitations. The new setup should fit on a 45 x 45 cm breadboard, while having at least the same stability, visibility and detection efficiency.

2. Digital Data Acquisition: Previously, all measurements were taken with an oscilloscope. When implemented into a complex experiment, the data acquisition and processing should be automated to run as part of sophisticated measurement sequences. In order to achieve such flexibility, an electronic data acquisition card should be implemented in the setup.

3. Data Analysis: While in principle a well known concept (see [7], [5]), a complete practical approach to state tomography that takes the measured voltages from the photodiodes in the interferometer and reproduces a density matrix in the Fock-Basis still has to be implemented.

2 Building and Characterizing An Interferometer

This chapter will first give an introduction on homodyne balanced detection and how that measuring method is realized with a Mach-Zehndner interferometer. Then the construction and tuning of the interferometer will be described. At last, the stability of the setup is analysed, using the Allan-deviation.

2.1 Theory of Balanced Homodyne Interferometry

This subsection is based on the sources [8], [11], [1], [3].

2.1.1 Concept of Balanced Detection

In balanced homodyne detection a strong reference beam, called the Local Oscillator beam (LO beam), is directed on a 50:50 phase-asymmetric beamsplitter.
As the splitting ratio is 50:50, two beams of equal power exit the beamsplitter. The two beams then hit two photodiodes behind the beamsplitter. Since both beams have equal power, both diodes give the same output signal and the difference signal between them is ideally zero, hence a balanced detection. The subtraction of the signals allows for very good cancellation of any technical noise from the diodes, as most technical noise signals should be identical in both diodes. Without light entering the beamsplitter from the other side, the difference signal will remain zero, up to some residual noise.
The beam entering the beamsplitter from the other side is called the probe beam. The probe beam enters the beamsplitter and will interfere with the LO beam and will disturb the balance. The disbalance causes a non-zero voltage and can therefore be measured. This is due to the phase-asymmetry of the beamsplitter. One reflection has a phaseshift of π and will interfere differently with the transmission on that side, compared to the other reflection that has no phase shift. The situation is depicted in figure 1. Assuming both beams had the same phase to begin with, the diode on top of the beamsplitter would see a reduced signal in this example, as the probe beam destructivly interferes with the LO beam, while the other diode´s signal increases due to the constructive interference. The interference term of the total power is proportional to the squareroot of the probe-power. This disbalance is only maximal, if both beams start at the same phase before entering the beamsplitter and zero, if they started with a phase difference of $\frac{\pi}{2}$. Thus the variations in the difference signal contain information about both the phase and amplitude of the probe-beam.

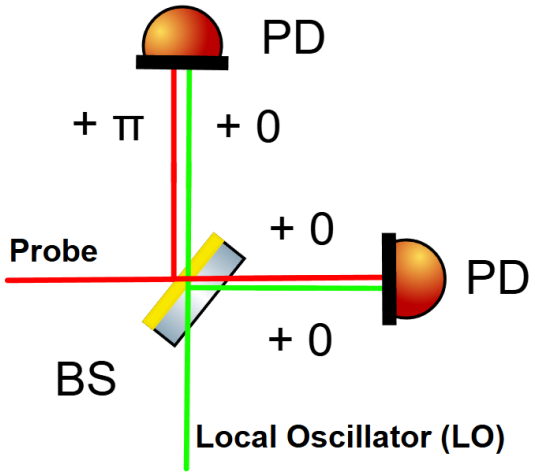

Figure 1: Schematic Layout of balanced detection. Probe beam in red, Local Oscillator in green. Different colours and spacing only for visualization. In the real experiment, the beams overlap and have the same wavelength. BS: Beamsplitter; yellow rectangle indicating dielectric coating; only the reflected probe beam picks up a $+\pi$-phaseshift. PD: Photodiodes; the substracted voltages give the difference signal, which is of intrest for state reconstruction.

Since the balanced difference signal is (apart from remaining noise) zero, a large amplification can be used for the difference signal without saturating any used amplifiers. This makes it possible to detect deviations from the LO-balance even by a few photons, making this detection method suitable for modern experiments in atomic physics, where signals are often just comprised of few photons.

2.1.2 Using A Mach-Zehndner-Interferometer For Balanced Homodyne Detection

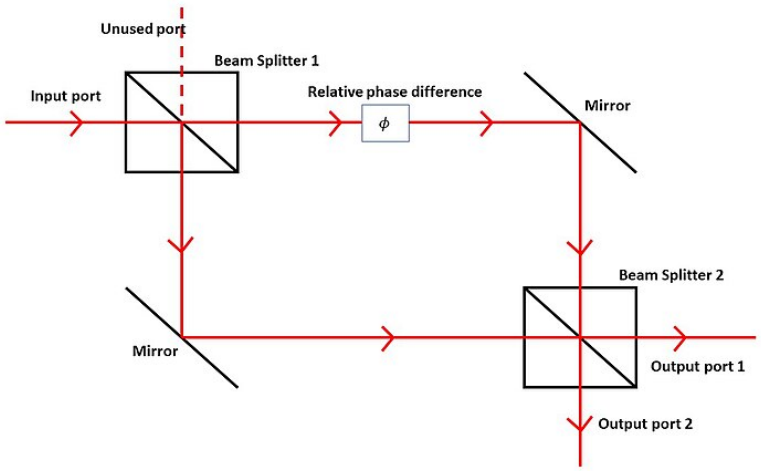

Figure 2: Schematic Layout of Mach-Zehndner-Interferometer; Relative Phase Differenc often comming from a probe. Imagesource: [6]

Homodyne interferometry means that both the reference LO-Beam and the probe beam have the same frequency. The easiest way to achieve this, is to create both beams from the same light source with a beamsplitter. The phase at the second beamsplitter depends on the pathlengths and any optical media in the path.
This combination of just two beamsplitters is called a Mach-Zehnder-Interferometer, which is shown in 2.
The orientation of the beamsplitters does not matter. Whether both coatings face in one direction, or in opposite directions, results in the same qualitative outcome. Flipping the relative orientation just changes which photodiode measures the constructive interference. The phaseshift of the first beamsplitter is unimportant, as it is just there to create two beams from the same source.

The most common application of a Mach-Zehndner-Interferometer is the analysis of a probe, which is placed in the probe beam. The interaction of the beam with the probe causes both attenuation and a phase shift, which alters the interference at the second beamsplitter and hence causing a disbalance in the difference signal, which produces the desired output signal. The phase shift and attenuation encodes information that allows insights into the nature of the probe.

2.2 Construction of the Homodyne Interferometer

This subsection will explain the components used in the setup and their function.

2.2.1 New Design Of Homodyne Interferometer

The setup that was build during this thesis, is shown in figure 3.

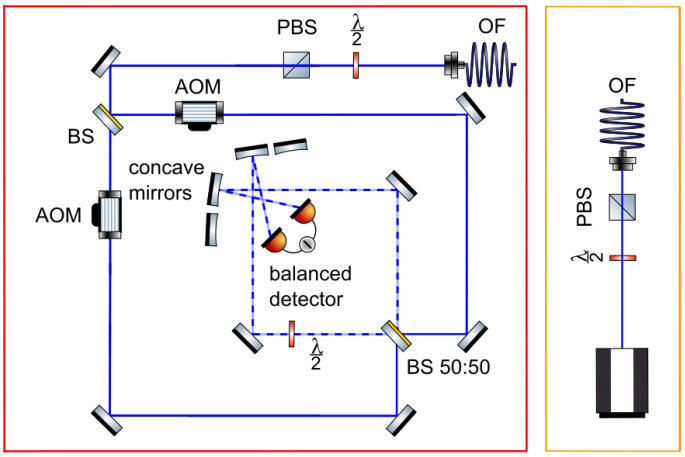

(a) Inkscape-Plot of Balanced Homodyne Interferometer. Light source is a laser emitting 399 nm. PBS: Polarizing Beam Splitter; OF: Opitcal Fibre; BS: Beamsplitter; AOM: Acousto Optical Modulator; Components in red and orange boxes are on different tables

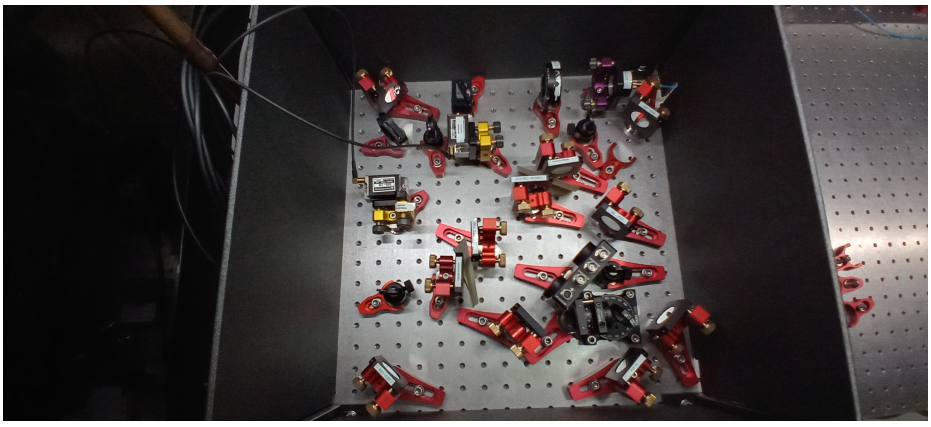

(b) Photo of Balanced Homodyne Interferometer; corresponding to red box in the sketch above)

Figure 3

The interferometer consists of three stages:

- The incoupling stage
- The splitting stage (LO- and probe-arm)
- The recombination unit

All components are mentioned in order of propagation. For brevity, all planar mirrors for aligning the beams are not mentioned. A list of the components and links to their full spec sheets is given in table 5 in the appendix.

The incoupling stage prepares the light for use in the interferometer. The light source for this experiment is a 3 Watt, 399 nm, cavity locked laser. At the fibre input, a $\frac{\lambda}{2}$-waveplate and a polarisation cube are used to control the power incoupled, sending a fraction of the output (up to 40 mW) through a polarisation-maintaining fibre (see orange box in figure 3). Another $\frac{\lambda}{2}$-waveplate and a polarisation cube after the fibre are used to controll the polarization in the interferometer.

The splitting stage consists of a beamsplitter that divides the light into two arms: the Local Oscillator (LO) arm and the probe arm. In both arms an Acousto Optical Modulator (AOM) allows variations of frequency, phase and intensity. The frequency shift, while not used for homodyne detection, is useful for a visibility measurement, which is explained in paragraph 2.3.3. The phase shift is strictly necessary for the tomography, as a full set of information about the probe beam can only be obtained when scanning the whole phase of 2π. This is due to the fact, that both a shift in phase and a shift in amplitude can both alter the interference (See 2.1.1).

The recombination unit overlaps the LO- and Probe-Beam at the second beamsplitter. The beamsplitter is mounted on a precision rotation mount, to ensure a splitting ratio as close to 50:50 as possible. The rest of the recombination unit consists of mirrors that guide the light to the two photodiodes. The final mirrors are curved to focus the light on the diode. An additional $\frac{\lambda}{2}$-waveplate is used in one path of the recombination unit, to artificially introduce small losses in one beam to get even closer to the desired power balance of the two arms.

The detector has three outputs: one for each diode and one difference signal. The individual diode-signals are first subtracted and then amplified. This allows the read-out of difference signal (RF-Signal), even when the individual amplifiers of the diode are saturated. The diodes have an equal efficiency to have the desired substraction to a signal close to zero, if both beams are of equal power.

A drawback of this setup is the high amount of photons, that are reflected off the diodes at 399 nm. Additional curved mirrors are placed in the beam path of the reflected light from the photodiodes. However these are not used in this iteration and are blocked.

In this iteration the two arms are constructed identically. In the future, the bottom left arm will serve as the probe arm. A fibre incoupler and outcoupler will replace the bottom left mirror and send the probe beam through a vacuum chamber.

2.2.2 Electronic Data Acquisition

To further automate the data acquisition, an Electronic Data Acquisition Card was installed. The card allows the simoultanious acquisition of two channels, which each have two different physical input impedances (50 Ω and $M1\,\Omega$). The noise characterization of the card is included in 3.2. For now the card is used exactly as a normal oscilloscope, with a GUI-Interface to select and start measurements.

The key advantage of the card is the option to programm the card and start measurements automatically within the framework of pulse sequences in the experiement the interferometer is later used.

2.3 Fine Tuning Of Components

It is no surprise that simply placing the right components in the right place is not enough. Certain steps are necessary to ensure proper function. While cumbersome and certainly needing some practice, only the most basic description of the process shall be mentioned here for brevity.

2.3.1 AOM-Efficiency

At first, the AOMs need to be properly installed, to ensure a high diffraction efficiency. AOMs are driven by an external signal generator. Sufficient repair and maintenance is necessary to ensure proper function of the AOMs.

Despite these hurdles, the AOM efficiencies could be brought to over 85 %, despite the manufacturer only promising 80 % for optimal conditions.

2.3.2 Balancing The Diodes

The next step is the balancing of the photodiodes. With the probe beam blocked, the Difference Signal should be zero, up to some noise (The noise will be talked about later). To achieve this, the beamsplitter is rotated to give a power metre reading equal in both arms, as a first rough alignment. Then, using the focal mirrors, the focal point is carefully centred on the diode. Then the beamsplitter is rotated to get the difference signal closer to zero. This will move the focal points of centre. The steps of focussing the light on the diodes centre and rotating the beam is done iteratively, until the minimal difference signal is achieved.
Then the additional $\frac{\lambda}{2}$-Waveplate is used to turn the polarisation of the stronger beam. Since the reflection of the diodes is dependent on the polarisation, losses can be introduced, by increasing the light reflected.

The balancing must be stable. Even changing the pointing by a fraction of a degree for example a mechanical vibration is moving a mirror back and forth, could result in a fluctuating difference signal. For this it is crucial to have the AOM at its maximal efficiency at a given RF-Power. The overall efficiency does not really matter, but it has to be at its local maximum, regardless of how good that maximum is. At the the maximum, one can be sure that the acoustic column is hit in the centre. Any change in pointing before the AOMs could lead to misalignment of the AOM to the beam and result in the beam not hitting the acoustic column in the centre and the resulting beam shape can be distorted. This can affect the balancing. If both the AOM and the Photodiodes are hit perfectly in the centre, slight deviations of the pointing, which are unavoidable to some extent, will not move the beam outside the area of the acoustic column or the photodiode, making the difference signal stable up to some residual noise.

2.3.3 Visibility

The final adjustment needed, is the mode matching between the LO- and probe-beam. Both frequency and polariziation are matched, as both beams originate from the first beamsplitter and the AOMs induce an equal frequency shift. The temporal mode (i.e. the pulse shape) is also automatically matched, as both beams are continous. This leaves only the spatial mode matching.

For a first rough alignment, beamwalking is used to overlap the LO- and probe-beam at the second beamsplitter. With a slight detuning in frequency via one of the AOMs, a beating voltage signal can be generated, giving a more sensesative alignment method.

If both the LO- and probe-beam have the same power and are perfectly mode matched, the amplitude of the oscillation should be maximal: The maximum voltage is at four times the individual amplitude and the minium is zero. As the voltage output from the diodes is directly proportional to the power of the light, the visibility can be calculated with the following equation:

$$Visibility = \frac{I_{max} - I_{min}}{I_{max} + I_{min}} = \frac{V_{max} - V_{min}}{V_{max} + V_{min}} \tag{1}$$

As a frequency detuning between arms, a beating frequency of 100 kHz was set. Small frequencies up to 1 kHz are too noisy and at higher frequencies the AOMs can slightly change the pointing of the beams. A fit function of the following form was used:

$$v(t) = a \cdot \sin(b \cdot t + c) + d \tag{2}$$

the visiblity in terms of the fit paramters is simply:

$$Visibility = \frac{a}{d} \tag{3}$$

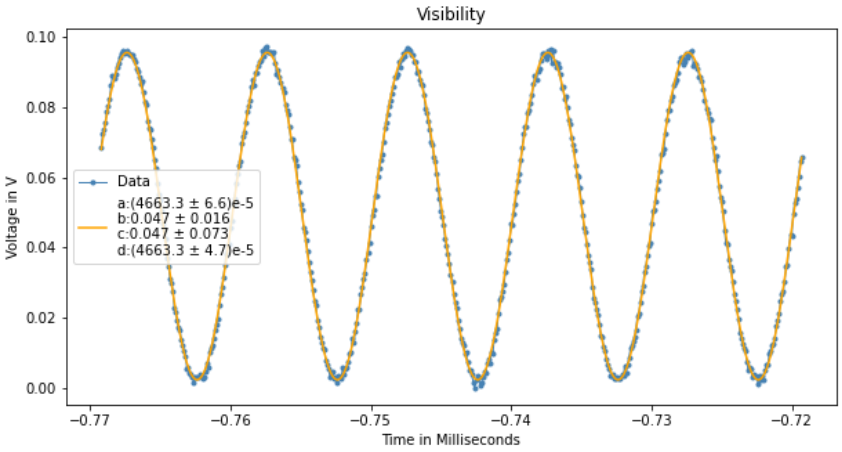

Figure 4: Measurement of Visibility. Beating of 100 kHz, recorded with 100 MS/s. Fitfunction according to equation 2.

The fit of the function is shown in figure 4. The resulting visibilty is 95 %. This is sufficient for homodyne tomography.

2.4 Stability-Measurement With Allan-Deviation

Another key feature of analysis is the stability of the setup. The sensitivity to pointing was eliminated for the balancing. However, there is a far greater phase-sensitivity. While the pointing only

significantly changes when components bend by a few micrometers, any distortion on the level of a few hundred nanometers is enough to completely change the phase difference between the arms. These mechanical virbration are dampened as good as possible, with the breadboard being on rubber feet on top of a floating table. To avoid any disturbances by airflow, a cardboard box was build around the interferometer.

To quantify the stability, the Allan-Variance is a usefull quantity. The approach taken here is based on previous measurements of the previous iteration of the interferometer [2]. When taking a voltage timetrace, the Hilbert-Transform can be used to calculate a function, from which the instantanous amplitude and phase of the signal can be calculated:

$$f(t) = V(t) + i\mathcal{H}(V(t)) \tag{4}$$

- $V(t)$: The Voltage-Timetrace
- i: imaginary unit
- $\mathcal{H}(V(t))$: Hilbert-Transform of the Voltage-Timetrace

Now with the phase of the timetrace known via $\phi(t) = arg(f(t))$, an Allan-Deviation-Plot can be produced. The Allan-Deviation measures how much the phase fluctuates between time windows of different sizes: If the phase is averaged over a time-interval τ, how much variance is there between the time-windows of size τ? This variance is then plottet against τ.
While in theory an instantanous phase can be derived for non-harmonic-signals, the analysis works better, if the signal is harmonic. To achieve this, a beating was introduced in the interference signal of the LO- and probe-beam, just like for the Visibitlity-Measurement (see 2.3.3), resulting in a sinusiodal voltage-signal.
The Allan-Deviaton-Plots were taken in different conditions, to see the effect of different beating frequencies and not closing the box. All measurements were recorded with 9 million samples (9 MS) with an acquisition rate of 100 megasamples per second (MS/s).

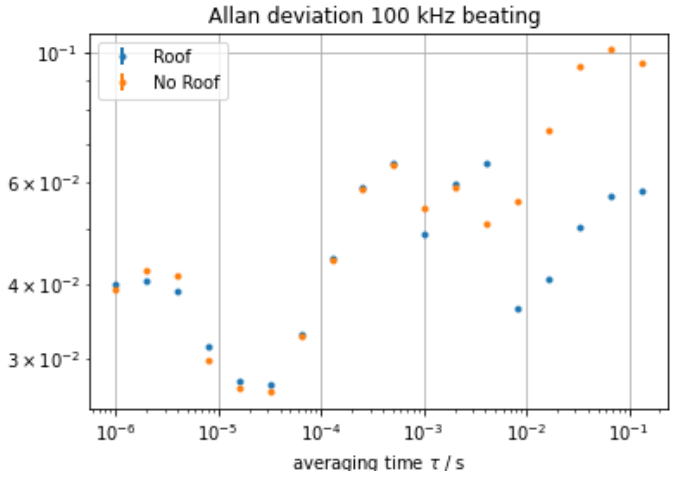

Figure 5: Allan-Deviation, Beating of 100 kHz, 9 MS recorded with 100 MS/s

As can be seen in figure 5 putting the roof of the cardboardbox on, helps to reduce instabilities, especially at low frequencies. There is still a peak in the milisecond regime and another one towards the longest avering times at 10^{-1} s. This approach did not take the time to thermaly stabilize the setup, after closing the roof and then the closures of the experimental tables.
All tables are cooled, so for the next experiment 3 Minutes were allowed to thermaly stabilize the setup, after sealing the enclosure. The resulting improvement can be seen in figure 6.

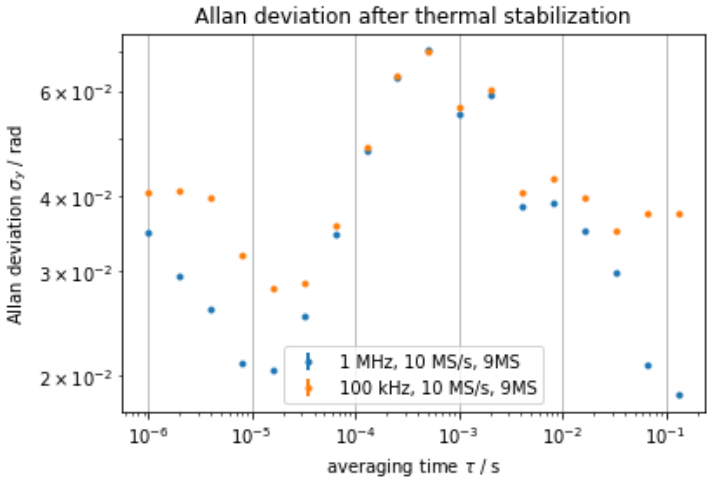

Figure 6: Allan-Deviation; Beating frequencies of 100 kHz and 1 MHz, 9 MS recorded with 100 MS/s

The peak in the milisecond regime is still there, but towards lower frequencies, the stability is greatly improved. This is expected, as air currents from thermal convection usually introduce distubances around 1-100 Hz.
Using the Allan-Deviation with a harmonic signal is generally easier, but still not without errors. The beating frequency can imprint itself as an artefact from numerical calculations. To test this, the beating frequency was changed from 100 kHz to 1 MHz.

The prominent peak in the milisecond-regime indicates a mechanical resonance. To check for such resonances, the beating was switched of and the difference signal was put on an spectrum analyser. The spectrum of the noise was analysed and a peak at 939 Hertz was visible, but only prominent when playing music with a speaker next to the setup or playing a pure 939-Hertz-Signal. A similiar resonance was identified in the previous design of the interferometer, at 850 Hz [2].
The source of the resonance could not be identified. But it is most likely a resonance of the whole breadboard, as damping individual components with a rubber did not change the frequency response.

The stability is sufficient in most cases for state reconstruction. Problems can occur, when the probe beam is pulsed on the timescale of milliseconds, where the prominent peak in instability occurs.

3 Quantum State Tomography

Whereas the measurement of many physical quantities like voltage, temperature or the speed of an macroscopic object are often trivial, measuring a quantum state is more complex. Especially the probabilistic nautre of Quantum Mechanics makes measurements difficult to perform, as the same experiment has to be repeated enough times, to infer the probabilities of the quantum state.
Quantum State Tomography is a method to fully measure a quantum state's characteristics. As with any attempt to reconstruct a probabilty distribution, the quantum state must be reliably constructed enough times, to infer the proability distribution from a decently sized set of measurements. Infering the probability distribution from the measured data is no trivial task. The algorithm used in this thesis for this reconstruction is based on the Maximum Likelihood Principle.

This chapter will first introduce the mathematical objects that appear in the algorithm, then explain the algorithm itself and then present the real measurements done by the interferometer, which were analysed by the algorithm.

3.1 Theory

This subsection describes the physics behind the mathematical objects, that describe the optical quantum states. For further reading see sources [7], [5], [9].

3.1.1 Density Matrix

The first mathematical object introduced to describe a quantum states is usually the wavefunction. However, the wavefunction is not capeable of describing all quantum states. The density matrix is a more powerful tool for that. Every wavefunction can be used to construct a density matrix:

$$\rho = |\psi\rangle\langle\psi|$$

However, there are some density matrices that can not be decomposed into a wavefunction.
The diagonal entries of the density matrix give the probability of being in the corresponding eigenstate. The off-diagonal elements give information on how these eigenstates are combined in ensembles and superpositions.

$$\rho = \begin{pmatrix} \rho_{11} & \rho_{12} & \cdots & \rho_{1n} \\ \rho_{21} & \rho_{22} & \cdots & \rho_{2n} \\ \vdots & \vdots & \ddots & \vdots \\ \rho_{m1} & \rho_{m2} & \cdots & \rho_{mn} \end{pmatrix}$$

As the density matrix contains all the information of a quantum state, the quantum state tomography will aim to reconstruct this matrix.

3.1.2 E-Field-Operator

To understand how the interferometer measures quantum effects of the electric field, a brief description of how electric fields are described in quantum mechanics.
Every Electrical Field can be described as a superposition of simple fields, like plane waves,

spherical harmonics or any other complete set of functions. For optical waves it is convinient to use a decomposition of simple plane waves. This can achieved by the E-Field Operator

$$\hat{\mathbf{E}}(\mathbf{r},t) = i\sum_{\mathbf{k},\beta}\left(\frac{\hbar\omega_{\mathbf{k}}}{2\epsilon_0 V}\right)^{1/2}\left(\hat{a}_{\mathbf{k},\beta}\mathbf{e}_{\mathbf{k},\beta}e^{i\mathbf{k}\cdot\mathbf{r}-i\omega_{\mathbf{k}}t} - \hat{a}^{\dagger}_{\mathbf{k},\beta}\mathbf{e}^{*}_{\mathbf{k},\beta}e^{-i\mathbf{k}\cdot\mathbf{r}+i\omega_{\mathbf{k}}t}\right) \tag{5}$$

In this formula k denotes the amplitude of the wavevector, which is related to the frequency of the light. λ: Enumerates the different possible polarizations The different polarisations are enumerates by β. The position and time at which to evaluate the field are denoted by r, t. $\mathbf{e}_{\mathbf{k},\beta}$ is the polratization vector and $\epsilon_0 V$ is a normalization constant, that is dependend on parameters of the experiment. The operator character comes from the ladder opperators:

- $\hat{a}_{\mathbf{k}}$ The annihilation operator
- $\hat{a}^{\dagger}_{\mathbf{k}}$ The creation operator

Any complicated state $|\psi\rangle$ can now just be given as a vector of coefficients for the plane-wave-decomposition. For example this list of coefficients n can easily be written for a coherent state like:

$$|\alpha\rangle = e^{-\frac{|\alpha|^2}{2}}\sum_{n=0}^{\infty}\frac{\alpha^n}{\sqrt{n!}}|n\rangle$$

The coefficients can be interpreted as the number of photons occupying the state of the n^{th} plane wave. The more photons are in a particular mode, the more it dominates the overall electric field. Instead of keeping track of each complicated electric field of all the modes, one simply keeps track of the number of photons in each mode and only applies the E-Field-Operator, when one is interested in the actual field configuration. To understand most physical processes like thermal radiation or pumping, one does not have to know the E-Fields involved, but just the statistics of occupation numbers. This trick of hiding the complexity of the field-geometry behind field operators is called second quantization. Representing states only by their occupation numbers, is called the Fock-Representation.

The Fock-Basis, sometimes called Occupation-Number-Basis, is a very common basis to do multi-particle quantum mechanics and lays down the foundation for Quantum Field Theory. It will be the Fock-Basis, that will be used to write down the density matrix that the measurement wants to reconstruct.

The Electric field can now be described by the statistical moments of the Electric Field Operator, i.e. it´s mean, variance etc. in any state ψ:

$$\langle\psi|\hat{\mathbf{E}}(\mathbf{r},t)|\psi\rangle \tag{6}$$

$$\langle\psi|(\hat{\mathbf{E}}(\mathbf{r},t))^2|\psi\rangle \tag{7}$$

$$\langle\psi|(\hat{\mathbf{E}}(\mathbf{r},t))^n|\psi\rangle \tag{8}$$

This representation nicely shows a key feature of quantum fields: Their fluctuations. One might wonder what there is to measure about the vacuum state. The expected mean value of the field is zero. This is actually the case for all so called Fock states. Fock states are states, were only a single mode is excited. For example a single-photon Fock state $|1_{\mathbf{k},\beta}\rangle$ indicates that there is exactly one photon in the mode characterized by $(\mathbf{k}, \beta)$ and zero photons in all other modes. This can be expressed as:

$$|1_{\mathbf{k},\beta}\rangle = |0\rangle_{\text{all other modes}} \otimes |1\rangle_{\mathbf{k},\beta}$$

The vacuum state is the Fock state with the ground-energy. Despite there being no excitations, the variance is still non-zero even for the vacuum state:

$$Var(\hat{\mathbf{E}}(\mathbf{r},t)) = \langle 0|\hat{\mathbf{E}}^2(\mathbf{r},t)|0\rangle - \left(\langle 0|\hat{\mathbf{E}}(\mathbf{r},t)|0\rangle\right)^2 = \left(\frac{\hbar\omega}{2\epsilon_0 V}\right) \tag{9}$$

The flucations can be measured, for example if they interfere with other fields. The classical formula for interference is still valid, if one plugs in the E-Field-Operators:

$$\hat{\mathbf{E}}_R = \sqrt{\hat{\mathbf{E}}_1^2 + \hat{\mathbf{E}}_2^2 + 2\hat{\mathbf{E}}_1\hat{\mathbf{E}}_2\cos(\Delta\phi)} \tag{10}$$

The difference signal in the interferometer is only dependend on the interference term as the other terms are subtracted. Despite the fluctuations of the vacuum being independant from the strengh of the E-Field in the LO-Beam, the resulting *signal* produced by the vacuum in the interferometer is dependend on the LO-power.

3.1.3 Quadratures

The key issue of interpreting the difference signal of the balanced photodiodes in the interferometer is the interdependence of the phase and amplitude that both influence the difference signal. A change in the difference signal could have come from either a change in the phase or the amplutide of the probe beam. The experimental setup of balanced homodyne detection and why this interdependence occurs was described in section 2.1.1.
A helpful concept to use in this situation is that of quadratures. The optical state is described by a quadrautre X_θ, with two quadrature components $\hat{x}$ and $\hat{p}$:

$$\hat{X}_\theta = \hat{x}\cos(\theta) + \hat{p}sin(\theta)$$

$$\hat{x} = \frac{1}{\sqrt{2}}(\hat{a} + \hat{a}^\dagger)$$

$$\hat{p} = \frac{1}{\sqrt{2}i}(\hat{a} - \hat{a}^\dagger)$$

The electric field $\hat{E}(t)$ is the quadrature $\hat{X}_\theta$ times a proportionality factor $\mathcal{E}_0$, that is dependent on experimental parameters.

$$\hat{E}(t) = \mathcal{E}_0\left(\hat{x}\cos(\theta) + \hat{p}sin(\theta)\right)$$

Despite the E-Field being the more familiar and tangable physical quantity, quadratures are often more convinient to work with.

Quadratures are usefull when describing optical states that are created by overlapping optical modes. This is precisely the situation in the interferometer. The E-Field merely describes a singular configuration of optical modes, for example the LO- and probe-beam being exactly out of phase. The quadratures allow us to look at all possible configurations (here a phase from 0 to 2π) of the combined modes simultaneously. This is very similar to all possible mechanical modes of a pendulum being described in phase space. That is the reason why the quadratures are often named the equivalent of position and momentum for optical states. The similarities go further, as both are pairs of conjugate basis and both fullfill the canonical commutation relation.

Measuring the difference signal, which is proportional to the E-Field, at different phases maps out the Quadrature distribution of the opitcal mode. The phase in the formula is the phase-difference between the two arms, which can be scanned through with one of the AOMs. (See Section 2.2.1)

The final issue is the proportionality factor. The difference signal is measured in Volts, but the quadrature is dimensionless. The proportionality factor will be calculated from noise-measurements in section 3.2

3.1.4 Wigner-Function And Tomography

The last mathematical object to be defined is the Wigner function. The distribution of quadrature measurements descriped in the previous section can be modeled by a function that describes the probabilty distribution of the two quadratures: This is the Wigner-Function.
The Wigner-Function can be projected to each axis, giving the probability distribution of both quadratures. These projections are the squared Wavefunctions in both basis X and P. This is illustrated in figure 7

The idea of Quantum State Tomography is to measure slices of the wigner function and combine those 2D-Plots into a 3D-Plot. The direct combination of slices to reconstruct the Wigner Function, is the Inverse-Radon-Transform. While appearing to be the most straight-forward method, experience has shown, that this direct approach is prone to numerical instability.
The much more robust method is the Maximim Likelihood Reconstruction, where first the density matrix is reconstructed and the Wigner Function is then plotted, using the density matrix.

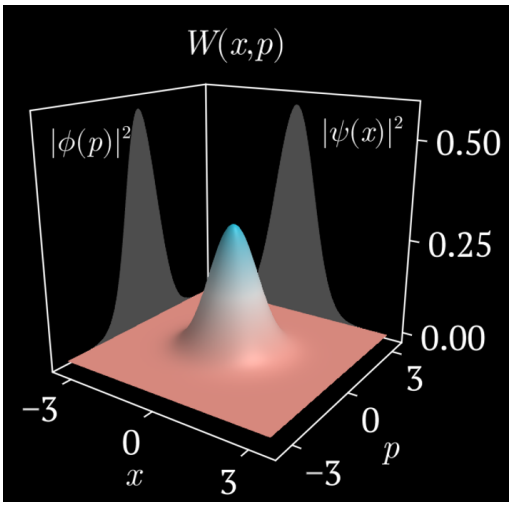

Figure 7: Illustration Wigner function of vacuum state. Axis are the quadrature components, and the projections the of the Wigner function on the axes give the probabilty distribution of the quadrature components. Imagesource: Extracted from [13]

3.2 Characterizing Noise

This section will first analyse the sources of noise and strategies to filter unwanted noise. Then the quantum-efficiency and the conversion factor from Volt to quadrature will be calculated from the vacuum shot noise.

3.2.1 Noise Sources

When measuring the vacuum (i.e.the probe arm of the interferometer is blocked), there are four types of noise in the difference-signal of the balanced photodiode:

$$\sigma^2_{full} = \sigma^2_{LO} + \sigma^2_{vac} + \sigma^2_{el} + \sigma^2_{card} \tag{11}$$

- Noise of LO-Beam: The LO beam will have technical fluctuations from instabilities of the laser. Any imperfections in the balancing means that noise from the LO beam is not perfectly canceled. The noise can have any arbitrary dependence on power or frequency, as it can be composed of several technical noise signals from the laser or other components in the beam. Most common is noise that is proportional to the sqaure of the LO power.

- Electronic Noise: This is the fundamental noise from electrical components. It is not being dependant on the laser power.

- Vacuum Noise: This is the noise that is to be measured for state reconstruction. This comes from the vacuum fluctuations and is therefore pure shot-noise. This noise is interfereing with the LO-Beam. As an interference signal, it is also dependend on the LO-power (see equation 10).

- Card Noise: Many papers count the noise from computer equipment towards electronic noise. However any electronic noise from cables or the diodes are, like all the previous

noise sources limited by bandwidth-filtering in the detection electronics, for example low-pass filters. However the electronics for measuring the signal, i.e. oscilloscopes or in this thesis the acquisition card can add additional noise to the data after any analog filters build into the electronics.

The hypothesis is, that noise of the LO beam should be sufficiently canceled and only play a role at higher powers, while the square dependence has minimal effects at low powers.
The electronic noise is the easiest term to handle. It has no dependence on the LO-Power. It quickly becomes dominated which sufficient LO-Power. Measurements where this is the case are often called shot noise limited.

To better understand the different noise sources, the signals were analysed with a Welch-Transform which is a modified Fourier-Transform and calculates the spectral power density [12]. At first the data acquisition card was terminated with 50 Ω. The card has no internal bandpass-filters and an analog input bandwidth of 250 MHz 5. This resulted in the plot shown in figure 8. The variance of that timetrace is $\sigma^2 = 1.243 \cdot 10^{-7}$ V^2, when . This is quickly dominated by other noise sources, but not negligible.

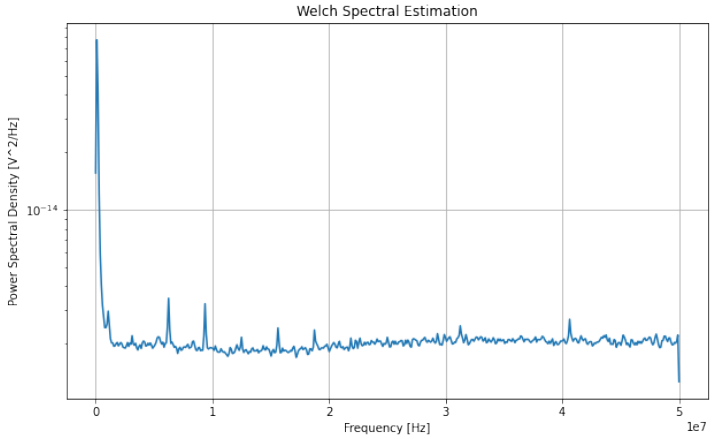

Figure 8: Welch spectral power estimation for card noise recorded with card input terminated with 50 Ω

The next step is to see, how the noise depends on the laser power. The spectral power density for several powers is shown in figure 9.

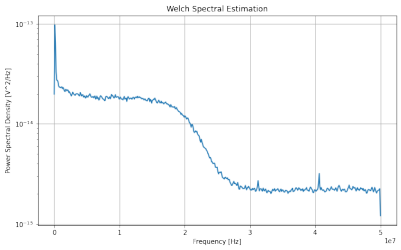

(a) Power of 200 μW

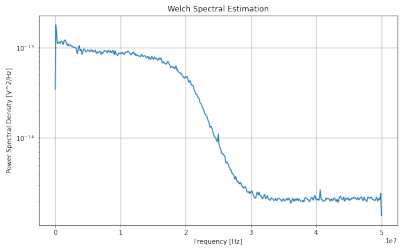

(b) Power of 4300 μW

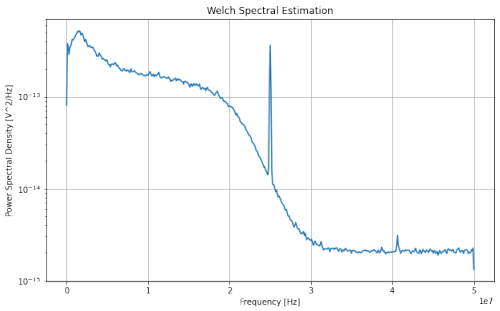

(c) Power of 8860 μW

Figure 9: Welch-Spectral-Power-Estimation at different LO-powers. Difference signal of balanced interferometer with blocked probe-arm. Signal attenuated with 15 MHz-lowpass-filter. A peak of 25 MHz is growing with increasing power, likely from a laser cavity modulated at that frequency. Additionlay there is some noise in addition to the white noise at low frequencies, either from another technical source, or as a mathematical relic of the Welch-Transform.

A peak grows at 25 MHz for increasing powers. This is most likely technical noise from the laser. The laser used is an infrared laser with a doubling cavity (see section on construction of setup 2.2.1). The modulation frequency of that cavity is 25 MHz, imprinting itself on the signal.

To get rid of such noise, a 15 MHz low-pass filter was build into the experiment. Any noise-signal with a much higher frequency than 15 MHz must have originated after the lowpass-filter and should be removed. However, analysis of the low-pass filter showed, that sufficient suppression is not achieved until 30 MHz, crucially not filtering the 25 MHz-Peak. Additionally the low-pass filter attenuates the voltage signal by a factor γ even at low frequencies. The analysis with a network analyser is shown in 10

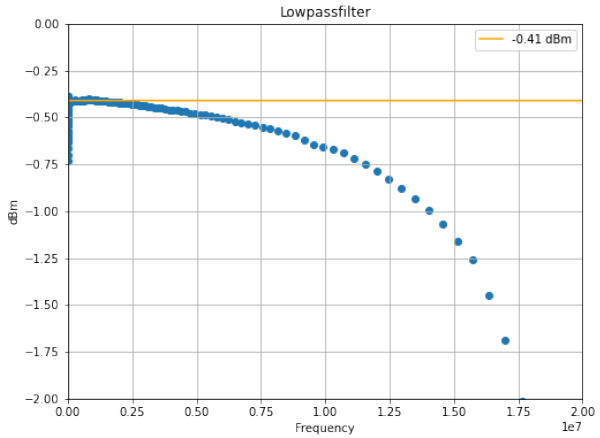

Figure 10: Analysis of low-pass filter with network analyser. Line indicating the attenuation for unfiltered frequencies.

With the cutoff not being sharp, the data must be filtered digitally:
One method is to average over a certain time-window. The period of of a 15 MHz signal is $T = 66.6$ ns. The voltage time traces in this experiment consist of over 4 Million samples with an acquisition rate of 10 ns per data point. Averaging over up to 6 points should only eliminate unwanted technical noise, while leaving the measured quantum noise untouched.
However, the averaging method is not introducing a lowpassfilter with a sharp cutoff. Therefore a digital lowpassfilter with a steep rolloff at 15 MHz was applied to all data using python-functions. The result can be seen in figure 11.

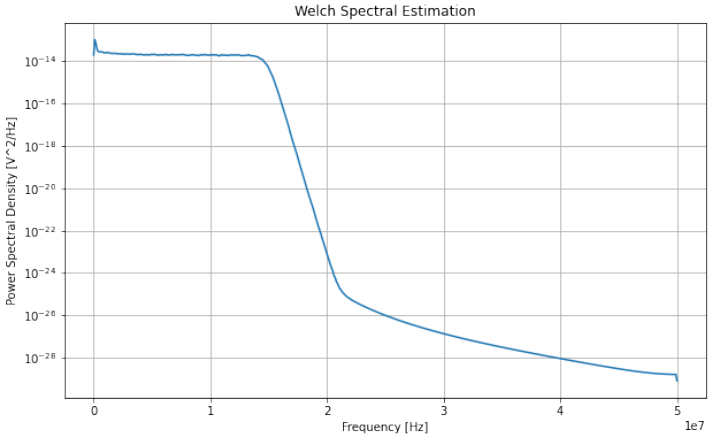

Figure 11: Spectral power estimation of digitally filtered signal using python functions.

With all these filtering measures, the variance of the voltage trace should first increase linearly with

the LO power and then have a square dependance at higher powers.
To confirm this, the noise is measured for increasing power. For powers up to 500 μW neutral-density filters were used. Above that threshold a waveplate and polarizing beam splitter placed before the fibre (see section 2.2.1) were used to vary the power.
The resulting graph is shown in figure 12.

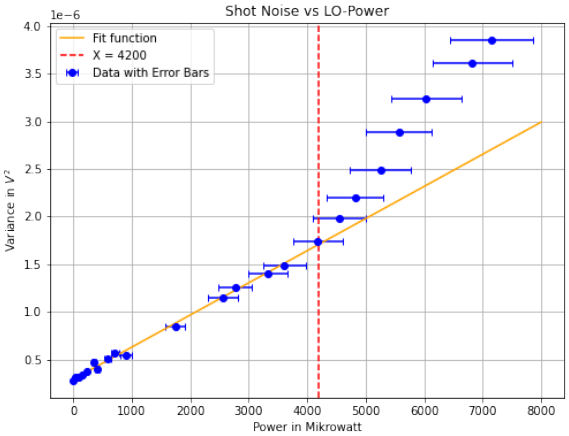

Figure 12: Variance of the difference signal of the balanced homodyne interferometer against power of the LO-Beam. Linear slope calculated by excluding the last seven data points (everything right of the red line). Parameters in equations 12 and 13

The resulting fit parameters are:

$$a = \left(3.367 \cdot 10^{-4} \pm 6.42 \cdot 10^{-6}\right) \frac{\mathrm{V}^2}{\mathrm{W}} \tag{12}$$

$$b = \left(2.97 \cdot 10^{-7} \pm 1.34 \cdot 10^{-8}\right) \mathrm{V}^2 \tag{13}$$

The noise scales linear up to 4.2 mW. Then technical noise that scales quadraticaly with the LO-power starts to dominate. Despite filtering out the 25 MHz-Peak, there is still some unwanted noise from the LO-beam. The source of that power-dependent noise could not be identified. The offset b is bigger than the card noise, which is expected as there is some additional electronic noise, from the cables and diodes.

Only the linear part defines the suitable power range for state reconstruction, unless one filters the data further. The slope of the linear part is needed for further calculations. A linear fit model was used to determine the parameters, while discarding the data-points from the quadratic part.

3.2.2 Quantum-Efficiency And Voltage-to-Quadrature Conversion

Before a tomography can be performed, the interferometer should be checked for a sufficient quantum efficiency. If too many photons are lost, a reconstruction could be faulty. Fortunatly the bar here is quite low and efficiencies above 20 % are already sufficient to reconstruct states reliably.

The value of the efficiency can then be used to calculate the conversion factor between quadrature and voltage.
The following analysis relies on formulas from [8]. However, there were some unit errors in the formulas in that source, so some modifications were made.

The voltage-operator is:

$$\hat{V}_\theta(t) = \sqrt{\frac{\eta_0 P_{\mathrm{LO}} q_e^2 \Delta\nu}{\hbar\omega_0}} \int G(\Omega) \left(\hat{a}_\Omega e^{i(\Omega t-\theta)} + \hat{a}_\Omega^\dagger e^{-i(\Omega t-\theta)}\right) \frac{d\Omega}{2\pi} \tag{14}$$

The quadrature operator is:

$$\hat{X}_\theta(t) = \frac{1}{G_0 \cdot \gamma \cdot \sqrt{2}} \int G(\Omega) \left(\hat{a}_\Omega e^{i(\Omega t-\theta)} + \hat{a}_\Omega^\dagger e^{-i(\Omega t-\theta)}\right) \frac{d\Omega}{2\pi} \tag{15}$$

Symbol	Variable	Value for this experiment
η	Quantum Efficiency	This is the variable to be calculated
P_{LO}	Power of the LO-Beam	Set in experiment
q_e	Elementary charge of electron	$1,602 \cdot 10^{-19} C$
ν	Bandwidth of data	15 MHz
$\hbar$	Planck's Constant	$6,626 \cdot 10^{-34} Js/2\pi$
ω	Frequency of the light used	751 THz $\times 2\pi$
G_0	Transimpedance gain	24500 V/A
γ	Attenuation factor of voltage amplitude	0.91

Table 1: Experimental Parameters

The voltage operator evaluated in the vacuum state is the shot-noise from quantum fluctuations:

$$\sigma^2 = \frac{\eta_0 \cdot 2G_0^2\gamma^2\Delta\nu q_e^2}{\hbar\omega_0} P_{\mathrm{LO}} \tag{16}$$

Measuring the slope of shot-noise vs. LO-power, allows one to extract the efficiency, using equation 16. Using the slope from 12. One gets an efficiency of $\eta = 46.1\%$. This is in agreement with previous measurements of the quantum efficiency for this setup [11].
The integrals in equations 14 and 15 are equal, allowing for the calculation of a voltage to quadrature factor:

$$\alpha = \frac{1}{G_0 \cdot \gamma \cdot \sqrt{2}} \cdot \sqrt{\frac{\hbar\omega_0}{\eta_0 P_{\mathrm{LO}} q_e^2 \Delta\nu}} \tag{17}$$

It is reassuring, that α has units of $\frac{1}{V}$. This factor can now be used to convert voltage-timetraces to quadrature-timetraces. However this conversion only holds true for the linear range. Even in the linear range, some residual influence of square terms may appear.

3.3 Maximum-Likelihood Reconstruction Of The Density Matrix

In this subsection, the algorithm will first be described and explained. Then the Fock-density matrix will be reconstructed from real data measured by the interferometer. It will be analysed how choosing different parameters of the algorithm, like number iterations and number of slices influence the result. While the interferometer is yet only capeable of measuring the vacuum state, an analysis on how to upgrade the setup to be able to measure arbitrary states is given at the end.

3.3.1 Iterative Algorithm for State-Reconstruction

For further reading see sources [7], [5].

The algorithm for the density-matrix-reconstruction only consists of multiplying matricies and a trace renormaliziation, which makes the algorithm numerically stable. One takes an initial guess for the density matrix, which in almost any case is the identity matrix of the desired dimension. This eliminates the task of choosing an inital guess in almost all practical applications. One only has to choose up to which Fock-Number the density-matrix shall be reconstructed. This initial guess is then multiplied by the so called R-Matrix, which is build from the experimental data and the current estimate of the density-matrix. For reasons to be explained at a later point, this gives the next estimate of the density matrix:

$$\rho^{(k+1)} = \mathcal{N}\left[\, R(\rho^{(k)})\, \rho^{(k)}\, R(\rho^{(k)})\right] \tag{18}$$

The $\mathcal{N}$ simply indicates the division of the Matrix by it‘s trace, to normalize it. Sufficient iterations converge on a best estimate for the density-matrix.
Calculating the R-Matrix such that it has the desired effect on the density-matrix, requires several calculations.
The calculation of the R-Matrix consists of three steps:

1. Convert the measured data into a histogramm of quadrature-measurements.
2. Calculate a so called projection matrix, that allows to predict the histogramm data from the current guess of the density matrix.
3. Put the projection matrix, the experimental data and predicted data together.

The measured data consists of one timetrace for each phase measured. The phase θ is the phase difference between the two arms of the interferometer (see section 2.2.1). The phases should be equally spaced between 0 and π. The phases will be numerated by the index i. The electronic acquistion records the difference-signal in Volts every few nanoseconds. The voltages for the vacuum state will gaussian distributed around zero. This means, that the device will record values close to zero for most measurements, with voltages further from zero being ever more rare. To reconstruct the gaussian-distribution, the code counts the number of datapoints within a certain voltage range. The bin-heights of these histogramms are the experimental data, that the reconstructed density-matrix has to predict. The bins in each measurement are numbered by the index j. So the total number of bin-heights $h_{i,j}$ is $i_{max} \cdot j_{max}$.

But how can a density matrix in the Fock basis predict the quadrature values? A projection matrix

is needed to asses how much the n-th Fock-state contributes to the probability of measuring the quadrature within the bounds of the j-th bin.
This is calculated by the overlap of the Fock number eigenfunctions and the quadrature eigenfunctions. The quadratures are continious variables like position. The optical modes follow the electromagnetic-wave-equation, which for plane waves transforms into the equation of the harmonic oscillator. This allows one to use the energy eigenstates of the quantum harmonic oscillator in the position representation to calculate that overlap:

$$\psi_n(x', \theta) = \langle x'|n\rangle = e^{i\theta n}\left(\frac{1}{2^n n!}\right)^{1/2}\left(\frac{m\omega}{\pi\hbar}\right)^{1/4} H_n\left(\sqrt{\frac{m\omega}{\hbar}}x'\right)\exp\left(-\frac{m\omega x'^2}{2\hbar}\right) \tag{19}$$

Where $H_n(z)$ is the n-th Hermite polynomial, m is the mass of the particle and ω is the angular frequency of the oscillator. Here x' is the position and still has units of space.
For massless light particles, the term $\sqrt{\frac{m\omega}{\hbar}} \cdot x$ is replaced with $2X_\theta$, where X_θ is the unitless quadrature. To fill the projection matrix $\prod_{i,j}^{m,n}$ of rank $m \times n$, for one certain bin, one integrates the product of the m-th-wavefunction conjugated times the n-th wavefunction, over the width of the bin :

$$\prod_{i,j}^{m,n} = \int_{a(j)}^{b(j)} \psi_m(X_\theta, \theta(i))^* \psi_n(X_\theta, \theta(i))\, dx \tag{20}$$

- a: X_θ-Value of lower boundry of j-th bin
- b: X_θ-Value of upper boundry of j-th bin
- θ: Phase of the i-th measurement

These integrals fill the projection matrix of rank $m \times n$. Since the phase-factor of $\psi_n(x, \theta)$ is the phase set in the measurement and the integral bounds depend on the quadrature-values spanned by a specific bin, each and every bin height $h_{i,j}$ gets its own projection-matrix. With this corresponding projection matrix, a theoretical value $t_{i,j}$ for the experimental bin height $h_{i,j}$ can be calculated for a given density matrix $\rho_{m,n}$ of rank $m \times n$:

$$t_{i,j} = tr\left(\prod_{i,j}^{m,n} \cdot \rho_{m,n}\right) \tag{21}$$

Now the density matrix must be optimized in such a way, that equation 22 becomes true.

$$\begin{pmatrix} h_{11} & h_{12} & \cdots & h_{1j} \\ h_{21} & h_{22} & \cdots & h_{2j} \\ \vdots & \vdots & \ddots & \vdots \\ h_{i1} & h_{i2} & \cdots & h_{ij} \end{pmatrix} \stackrel{?}{=} \begin{pmatrix} tr\left(\prod_{1,1}^{m,n} \cdot \rho_{m,n}\right) & tr\left(\prod_{1,2}^{m,n} \cdot \rho_{m,n}\right) & \cdots & tr\left(\prod_{1,j}^{m,n} \cdot \rho_{m,n}\right) \\ tr\left(\prod_{2,1}^{m,n} \cdot \rho_{m,n}\right) & tr\left(\prod_{2,2}^{m,n} \cdot \rho_{m,n}\right) & \cdots & tr\left(\prod_{2,j}^{m,n} \cdot \rho_{m,n}\right) \\ \vdots & \vdots & \ddots & \vdots \\ tr\left(\prod_{1,j}^{m,n} \cdot \rho_{m,n}\right) & tr\left(\prod_{2,j}^{m,n} \cdot \rho_{m,n}\right) & \cdots & tr\left(\prod_{i,j}^{m,n} \cdot \rho_{m,n}\right) \end{pmatrix} \tag{22}$$

This is where the R-Operator comes in. It will hopefully make both sides of equation 22 equal for high numbers of iterations of equation 18.
The ingredients for the R-Operator are now ready for assembly:

$$R = \sum_i \sum_j \frac{h_{i,j}}{t_{i,j}} \prod_{i,j}^{m,n} \tag{23}$$

The ratio $\frac{h_{i,j}}{t_{i,j}}$ indicates how well the theoretical and experimental value agree. A discrapency results in a scaling factor different from 1 for the density matrix. Since the entries of the density matrix contribute to the bin height differently, the projection matrix weights the scaling factor for each entry of the density matrix according to the overlap of the state measured and the state described by that entry.
As the density matrix is a (1,1)-Tensor, the projection has to be applied by multipling from both sides. This concludes the motivation behind equation 18.
The alogrithm has converged, when all theoretical and experimental values are in agreement.

3.3.2 Reconstructing The Density Matrix From RF-Data

With the interferometer build, the noise analysed and the algorithm prepared, one can finally measure and reconstruct the vacuum state. This subsection will first describe the measurement and then present the results for different parameters.

The measurement consists of blocking the probe-arm of the interferometer and measuring a voltage timetrace for each phase set by an AOM . The voltage timetrace take the photodiode signal from the RF-output, which is the difference signal (see section 2.2.1). As this is the measurement of the vacuum state, one does not expect the phase to make any difference, but just to make sure the AOMs work properly at all settings, the measurements were done with real differences in the set phase.

The the algorithm was used with the following parameters: From 0-180 degrees, 13 timetraces were used with a seperation of 15 degrees. The resulting histogramms were nearly identical and had a gaussian form. This can be seen for one such histogramm in figure 13. The variance is $\sigma^2 = 0.272$, which is fairly close to the theoretcial variance of the vacuum state of $\sigma^2 = 0.25$ [4].

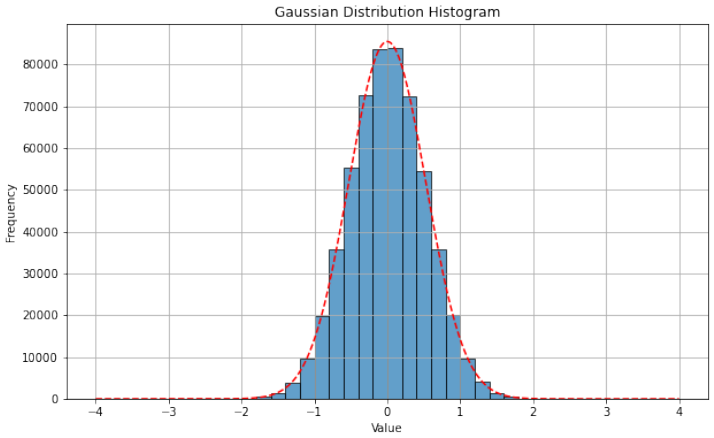

Figure 13: Histogramm of binned quadratures. Calculated from voltage timetrace of difference signal of the balanced interferometer with blocked probe beam (vacuum state). Conversion to quadrature with equation 17. Red line indicating a gaussian fit.

The algorithm was then run with 800 iterations of equation 18. The results are shown in figure 14.

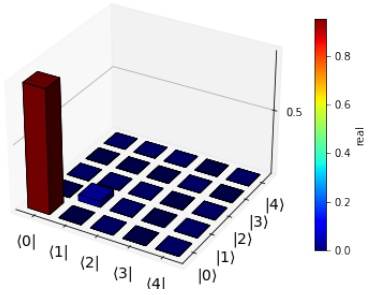

(a) 3D-Plot of density matrix

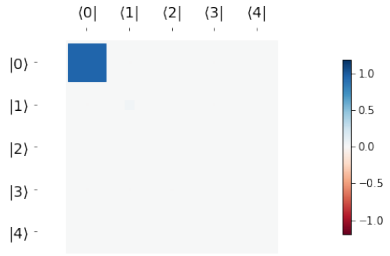

(b) Hinton Plot of density matrix

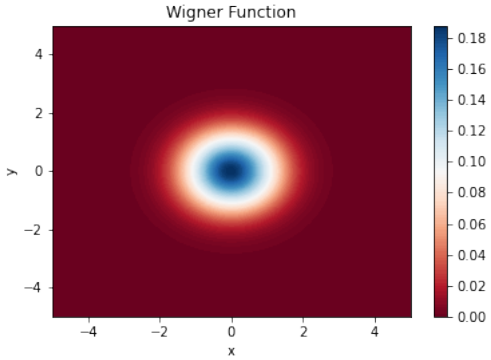

(c) Wigner function constructed from density matrix using QuTip [10]

Figure 14: Reconstructed quantum state using: 13 timetraces from 0-180 degrees in steps of 15 degrees. 800 iterations for matrix reconstruction, using equation 18. Calculated from voltage timetrace of difference signal of the balanced interferometer with blocked probe beam (vacuum state).

As expected, the (0,0)-entry of the density matrix is the only significantly populated state. Some minor occupation of the (1,1)-entry is present, most likely due to some unaccounted technical noise.

One might wonder, if so many timetraces and iterations are necessary for a decent reconstruction. Surprisinlgy the state can be reconstructed with far less rigid data. Even a few timetraces or just one iteration get very close to the expected result. This can be seen in figure 15.

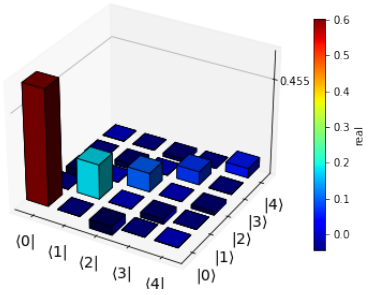

(a) 3D-Plot of density matrix with just one iteration of equation 18

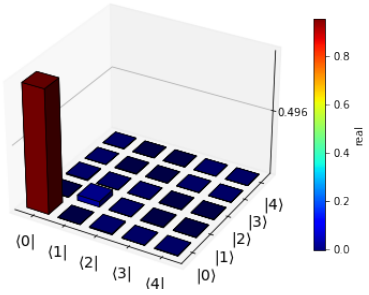

(b) 3D-Plot of density matrix 10000 iterations of equation 18

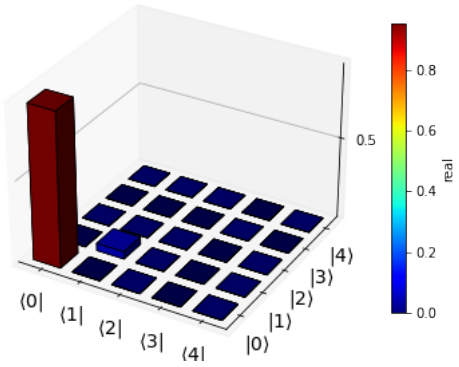

(c) 3D-Plot of density matrix with just three timetraces and 800 iterations of equation 18

Figure 15: Reconstructed quantum state different paramters. Calculated from voltage timetrace of difference signal of the balanced interferometer with blocked probe beam (vacuum state)

Despite the reassuring result, that the algorithm works for different settings, at least from a computational point of view, it is not really useful to cut down the number of timetraces or iterations. The number of timetraces slightly reduces the computational effort for the construction of the R-Operator. However, this part of the algorithm could be drastically improved with parallel computations of the integrals in equation 20. The number of iterations has a negligible effect on the overall runtime.

3.4 Towards reconstruction of other states

With the successful reconstruction of the vaccuum state comes the question of how to reconstruct other states. Apart from other Fock-states there are coherent states, thermal states, squeezed states and many more. The procedure for the data analysis will stay mostly the same.

One key issue preventing the reconstruction of such quantum states is the lack of a phase reference: The phase difference between the two arms of the interferometer drift over time. If too much time passes between measurements of different phase-settings of the AOM $\Delta\theta$, the real phase difference between the arms is unknown.

The AOMs can only add a an additional phase difference $\Delta\theta$. But the absolute phase difference is unknown. This would not be a problem, if the absolute phase difference was stable. But as discussed in section 2.4, the interferometer has unescapeable mechanical noise, which translates into differences in the pathlenght and therefore the phase.
There is a certain time-window where the phase drift is in a accepteable low range. If one first measures the absolute phase and then within that timewindow adds one or more phases through the AOM and then performes the data aqcuisition, the phase is known with sufficient precision.
However, the absolute phase can only be measured with a strong probe beam, while the final experimental use in an optics lab with ultra-cold atomic gases requires only a few photons in the probe beam. A mechanism on how to switch between the intensity for reference measurements and the main measurements must be found. The challenge is, that this switching must not change the pointing, as even the slightest change in beam pointing can severly affect the visibility, stability and balance.
Another option, at least for simple measurements is the rapid acquisition of of all data within a stable time window. However this is only an option, if one wants to measure sufficiently short experiments. Even this method is currently not possible, as the phase is selected with a GUI-Programm, where the phase is typed in by hand. This obviously takes much longer than any safe time window. To proceed with any measurements, that involves knowing the phase, a method must be designed to automatically set the phase by a programm that can directly communicate with the electronics generating the RF-Signal for the AOM.

The first idea to allow a switch in intensities, is using AOMs. Using AOMs that are fed changing RF-Power to go from low diffraction efficiency (for main measurements) to high efficiency (for reference measurements) is not possible with the current AOM-Models at hand. Rapidly switching between different RF-Signals does not allow for enough time to bring the AOM to thermal equilibrium. This will cause unpredictable changes in efficiency and pointing.

Another option is to overlap a strong beam with the probe beam, when needed. This additional beam would need to be created with a beam splitter from the original source to ensure the same beam-profile, intensity-fluctuation etc. This additional beam could then be switched on and off with a beam shutter.

4 Summary & Outlook

Out of the three challenges approached in this thesis, two have been mostly resolved. The interferometer is now placed on a small portable breadeboard and still has a visiblity of 95 %, a quantum efficiency of 46 % and an Allan-Deviation, that is in the range of $\sigma_{allan} = (4 \pm 3) \cdot 10^{-2}$ from timescales of seconds to microseconds.
Some minor improvements could still be made to the efficiency and stability.
Up until now the extra mirrors rereflect light that has been reflected of the didoes have not been used. One has to consider, that the increase in efficiency is introduces extra instability to the balance, especially given the fact the efficiency of the setup is already well within the execptable range for state reconstruction.
So far the source of the prominent 939 Hz mechanical resonance of the setup could not be identified. It is likely, that it is a resonance of the whole breadboard/table and can therefore not be completly eliminated. The resonance influences the stability on timescales that are not that relevant to the main experiment and the resonance is only strongly excited with loud sounds that contain 939 Hz.

The digital data acquisition is still in the early stages. The data acquisition card has been installed and the firmware has been tested, but this only includes GUI-Interfaces with limited options. An automated script, that triggers measurements and then analyses the datastream needs to be designed. Part of that script must be an automated mechanism, that sets the phase of the interferometer.

The practical tools for state reconstruction are ready for usage. The convesion factor from voltage to quadrature can be calculated and the tools for density matrix reconstruction have been programmed. The width of quadrature measurements was in agreement with the theoretical results. The vacuum state could be reconstructed and the alogrithm was tested to robust against changes to parameters.

The long term goal of implementation in the main experiment with ultra cold atomic gases then requieres the redirection of the probe beam trough the vacuum chamber and an implementation of a phase reference.

5 Appendix

Component	Name	Specifications
AOM	AOM 3200 129 Goose & Hoosego	AOM 3200 129 Specifications
Beamsplitter	Layertec Beamsplitter 108607	Layertec Beamsplitter 108607 Specifications
Balanced Detector	Thorlabs PDB230A	Thorlabs PDB230A Specifications
Acquisition Card	RazorPlus Express 16-Bit Digitizer	RazorPlus Express Specifications

6 Acknowledgements

At first I would like to thank the group as a whole. Everyone is super welcoming and happy to help. For a few people there are some extra words I would like to say a few extra words:
Thank you Eduardo for designing such an intersting and multifaceted project! I never would have thought, that I learn so much about programming, electronics and optics in just 4 months.
Thank you Tangi for stating in my first week "I will never get mad because of too many questions!". Despite my unintentional effort, I never surpassed the limit and regardless at what time or how obvious the answer was, you were always there to help!
Thank you Xin and Ludwig, for always cheering me up, if something did not work for the 20th time.
Thank you Wolfgang for the deep discussions! It massively improved my sleep quality to go home with less knots in my head :)

$$\frac{1}{1}\begin{pmatrix}1 & 0\\ 0 & 0\end{pmatrix} + \frac{0}{1}\begin{pmatrix}0 & 0\\ 0 & 1\end{pmatrix} = \begin{pmatrix}1 & 0\\ 0 & 0\end{pmatrix} \tag{24}$$

$$\begin{pmatrix}1 & 0\\ 0 & 0\end{pmatrix}\begin{pmatrix}1 & 0\\ 0 & 1\end{pmatrix}\begin{pmatrix}1 & 0\\ 0 & 0\end{pmatrix} = \begin{pmatrix}1 & 0\\ 0 & 0\end{pmatrix} \tag{25}$$

$$\rho_{initial} = \begin{pmatrix}1 & 0 & 0 & 0\\ 0 & 1 & 0 & 0\\ 0 & 0 & 1 & 0\\ 0 & 0 & 0 & 1\end{pmatrix} \tag{26}$$

References

[1] *A balanced homodyne detector and local oscillator shaping for measuring optical Schrödinger cat states*. URL: https://tsapps.nist.gov/publication/get_pdf.cfm?pub_id=908299 (**urlseen** 2024).

[2] Theresa Dewey. *Stability and Sensitivity Limit of a Few-Photon Homodyne Interferometer for Yb Quantum Optics Experiments*. Oxford Science Publications, 2024.

[3] *How does a Mach-Zehnder interferometer work?* URL: https://iopscience.iop.org/article/10.1088/0031-9120/35/1/308/pdf (**urlseen** 2024).

[4] Rodney Loudon. *The Quantum Theory of light*. Oxford Science Publications, 2000.

[5] A. I. Lvovsky **and** M. G. Raymer. *Continuous-variable optical quantum state tomography*. 5.11.2005.

[6] *MZ-Layout*. URL: https://commons.wikimedia.org/wiki/File:Mach_Zehnder_interferometer_schematic_diagram.jpg (**urlseen** 2024).

[7] *Numerical study of Wigner negativity in one-dimensional steady-state resonance fluorescence*. URL: https://journals.aps.org/pra/pdf/10.1103/PhysRevA.100.063808 (**urlseen** 2024).

[8] Alexei Ourjoumtsev. *Homodyne spectroscopy of a coupled cavity-atom system*. 2017.

[9] Peskin **and** Schroeder. *An Introduction to Quantum Field Theory*. CRC Press, 1995.

[10] *QuTip Wigner*. URL: https://qutip.org/docs/4.0.2/modules/qutip/wigner.html (**urlseen** 2024).

[11] Wayne Ströbel. *Constructing a Homodyne Detector for 399nm Laser light*. 2023.

[12] Peter Welch. *The Use of Fast Fourier Transform for the Estimation of Power Spectra: A Method Based on Time Aver. aging Over Short, Modified Periodograms*. IEEE TRANSACTIONS ON AUDIO **and** ELECTROACOUSTICS, 1967.

[13] *Wigner function for number states*. URL: https://en.wikipedia.org/wiki/Wigner_quasiprobability_distribution#/media/File:Number_state_Wigner_function.png (**urlseen** 2024).